18 June 1997
Electronics Letters Online No: 19970953

P. Charles (*Hewlett Packard Ltd., Ipswich Components Operation, White House Road, Ipswich, Suffolk, United Kingdom*)

References

1 VAN GURP, G.J., JACOBS, J.M., BINSMA, J.J.M., and TIEMEIJER, L.F.: 'InGaAsP/InP lasers with two RIE etched mirror facets', *Jpn. J. Appl. Phys.*, 1989, **28**, (7), pp. L1236–L1238

2 HICKS, S.E., WILKINSON, C.D.W., DOUGHTY, G.F., BURNESS, A.L., HENNING, I., ASGHARI, M., and WHITE, I.: 'Reactive ion etching of low-loss mirrors in InP/InGaAsP/InP heterostructures using CH4/H2/O2 chemistry'. Proc. ECIO, 1993, pp. 2-36–2-37

3 WILLIAMS, P.J., CHARLES, P.M., GRIFFITHS, I., CARR, N., REID, D.J., FORBES, N., and THOM, E.: 'WDM transceiver OEICs for local access networks', *Electron. Lett.*, 1994, **30**, (18), pp. 1529–1530

4 RING, W.S., LAGE, H., TAYLOR, A.J., SMITH, I.S., and ASH, R.M.: 'Optimisation of highly efficient uncoated strained 1300nm InGaAsP MQW lasers for uncooled high temperature operation'. Paper ThG4, Tech. Dig. OFC, 1995, pp. 230–231

5 FRANCIS, D.A., CHANG, C.J., and EASTON, K.: 'Effect of facet roughness on etched-facet semiconductor laser diodes', *Appl. Phys. Lett.*, 1996, **68**, (12), pp. 1598–1600

Improved 3D ray launching method for wireless propagation prediction

G. Durgin, N. Patwari and T.S. Rappaport

Indexing terms: Ray tracing, Radiowave propagation

3D ray tracing produces accurate, deterministic channel models for wireless system design. Increasing a ray tracing algorithm's ability to identify correct propagation paths reduces the *kinematic* errors of a simulation. A new 3D ray tracing technique is presented that reduces kinematic errors associated with ray launching algorithms.

Introduction: Ray launching techniques shoot rays from a transmitter location which are then reflected, diffracted, and scattered through a computerised environment. Launched rays that pass arbitrarily close to a receiver location are used to predict the actual propagation paths. Rays may be launched from the vertices of a geodesic sphere to provide unbiased 3D coverage and localised uniformity [1].

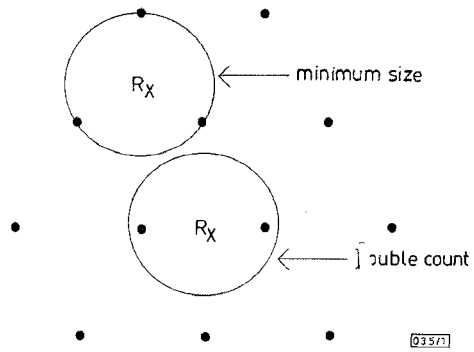

Fig. 1 *Reception sphere double counts on uniform, geodesic wavefront*

Reception sphere: A common method for interpreting the traced ray information is the reception sphere model. A sphere, centred on a candidate receiver location and sized according to the angular separation of the incoming rays, collects the rays that contribute to the overall electric field. Fig. 1 shows the ideal impingement of geodesic-launched rays onto a spherical wavefront. The minimum radius for a reception sphere to guarantee the collection of at least one ray from a wavefront is $1/\sqrt{3}$ of the distance between adjacent rays. This radius sweeps out a circular area across the wavefront where sometimes two rays fall within the sphere, registering additional field at the particular receiver location [2]. For a randomly placed receiver, these double count errors occur with a probability of $\frac{2\pi}{3\sqrt{3}} - 1$ or 20.9% of the time.

The angles of arrival and the path lengths of two rays from the same wavefront are identical. Since their amplitudes and phases are equal, they add coherently to register twice as much electric field: a +6 dB power error per wavefront. Assuming random location of a receiver across a single wavefront, a measurement with reception spheres will increase the mean power by at least 63% and introduce ±122% of additional standard deviation error. Even higher deviations have been shown in [3].

Distributed wavefronts: The method of distributed wavefronts remedies the double count problem inherent with the reception sphere model, while maintaining the speed and simplicity of ray launching. Instead of counting hit-or-miss rays, the contribution of nearby rays are weighted as a function of proximity to the receiver. Thus, the total electric field at any receiver point $\vec{r}$ is determined by a weighted sum of fields across each multipath wavefront:

$$\vec{E}(\vec{r}) = \sum_{i=1}^{N} \vec{E}_i f(x_i) \qquad (1)$$

Table 1: Tabulated values for distributed wavefront weighting function

x	$f(x)$	x	$f(x)$	x	$f(x)$
0.000	1.000000	0.350	0.755992	0.700	0.143627
0.025	0.997451	0.375	0.714609	0.725	0.114993
0.050	0.994310	0.400	0.670687	0.750	0.090079
0.075	0.989887	0.425	0.624725	0.775	0.068779
0.100	0.983723	0.450	0.577259	0.800	0.051053
0.125	0.975419	0.475	0.528856	0.825	0.036723
0.150	0.964567	0.500	0.480105	0.850	0.025471
0.175	0.950793	0.525	0.431592	0.875	0.016905
0.200	0.933756	0.550	0.383894	0.900	0.010621
0.225	0.913197	0.575	0.337574	0.925	0.006190
0.250	0.888966	0.600	0.293157	0.950	0.003215
0.275	0.861056	0.625	0.251151	0.975	0.001356
0.300	0.829511	0.650	0.211982	1.000	0.000000
0.325	0.794412	0.675	0.176035		

The vector $\vec{E}_i$ is the field associated with the ith ray. The weighting function is $f(x_i)$, where x_i is the normalised distance between the ith ray and the receiver location. A ray makes a non-zero contribution to the total field only if the receiver point is at a distance closer than the ray's nearest neighbour. The radially symmetric weighting function in Table 1 is designed to produce a very accurate field result for the case of a uniform spherical wave. If all of the rays on the geodesic wavefront pattern in Fig. 1 have the same field vector $\vec{E}_o$, then the weighted sum of nearby ray fields at any point on this wavefront will also be $\vec{E}_o$.

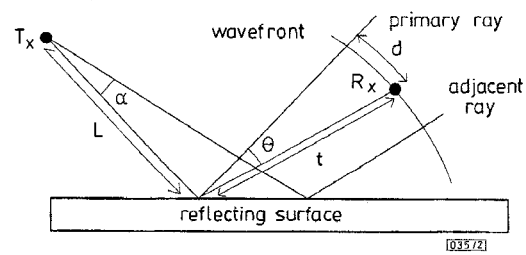

Fig. 2 *Side view of geometry for distributed wavefront*

This tabulated function weights field contributions based on the arc length from the receiver point to a nearby ray, shown as d in Fig. 2. Equations for the total distance travelled by the ray, R, and the normalised distance along a wavefront, x, are given by eqns. 2 and 3.

$$R = \sqrt{L^2 + t^2 + 2Lt\cos\theta} \qquad (2)$$

$$x = \frac{d}{\alpha R} = \frac{1}{\alpha}\tan^{-1}\left[\frac{t\sin\theta}{L + t\cos\theta}\right] \qquad (3)$$

The normalised distance x is a ratio of the distance d to the arc length between a ray and its nearest neighbour, as described by the geodesic ray launching geometry. It allows the distributed wavefront method to use the same weighting function given by Table 1 in the range $0 \le x \le 1$, regardless of the angular separation between rays.

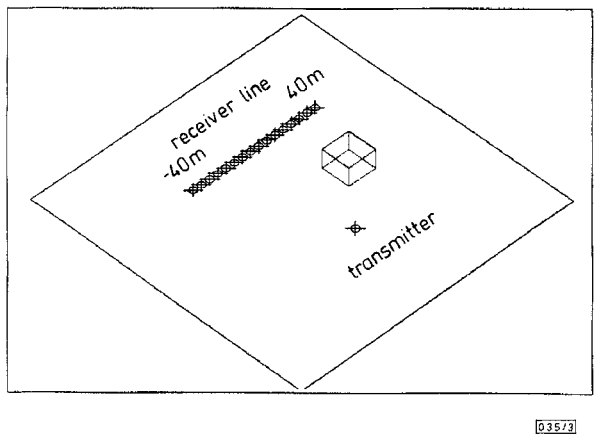

Fig. 3 *Receiver line placed in simple environment to compare ray tracing algorithms*

Results and measurements: Both reception sphere and distributed wavefront techniques were tested in a simple theoretical environment. The 3D scene, shown in Fig. 3, consisted of a flat plane with a single box-like building. All surfaces were assigned arbitrary reflection coefficients of –3dB. The geometrical optics fields of a 900MHz transmitter were modelled and a receiver line was placed on the far side of the building. Among the receivers was a group that received specular reflections from one side of the building, increasing the mean power level.

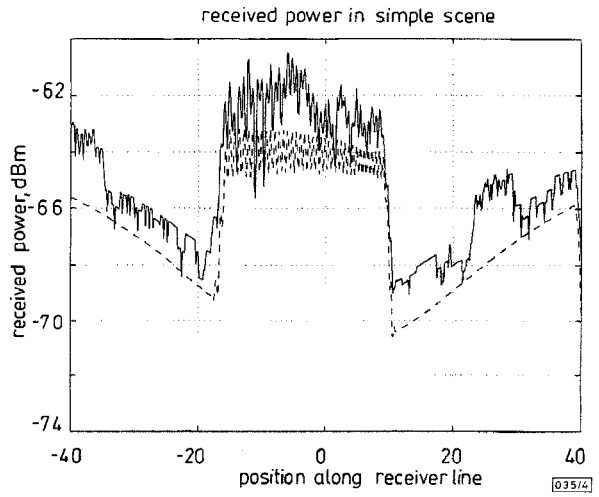

Fig. 4 *Power along receiver line using reception sphere and distributed wavefront methods (0dBm transmit power at 900MHz)*

Averaging window of 1m was applied to raw power predictions for clarity
– – – – distributed wavefront
——— reception sphere

Fig. 4 shows the received power along the line. For clarity, a small averaging window of one metre was applied to mitigate the erratic wave interference pattern. It is seen that the reception sphere method artificially inflates the mean power along the 80 m track and produces non-physical fluctuations absent in the distributed wavefront method. These fluctuations worsen for reception spheres in the region of increased illumination.

Conclusions: Geodesic spheres and distributed wavefront methods increase the accuracy of 3D ray tracing for propagation prediction by eliminating the kinematic errors of double-counting while maintaining simplicity and speed. The distributed wavefront method corrects the deviations in the reception sphere model. Unlike the reception sphere model, this new technique can model phasor-summed fields and produce accurate fading profiles. The method also lends itself to modelling non-uniform, astigmatic wavefronts and discrete 3D antenna patterns.

Acknowledgments: This work is sponsored by the NSF Presidential Faculty Fellowship under grant No. NCR9253598 and the MPRG Industrial Affiliates Program.

6 May 1997
Electronics Letters Online No: 19970928

G. Durgin, N. Patwari and T.S. Rappaport (*Mobile and Portable Radio Research Group, Bradley Department of Electrical Engineering, Virginia Polytechnic Institute and State University, 840 Pointe West Commons, University City Blvd., Blacksburg, VA 24061, USA*)

References

1 SEIDEL, S.Y., and RAPPAPORT, T.S.: 'Site-specific propagation prediction for wireless in-building personal communication system design', *IEEE Trans. Veh. Technol.*, 1994, **43**, (4), pp. 879–891
2 LAWTON, M.C., and MCGEEHAN, J.P.: 'The application of a deterministic ray launching algorithm for the prediction of radio channel characteristics in small-cell environments', *IEEE Trans. Veh. Technol.*, 1994, **43**, (4), pp. 955–969
3 TAN, S.Y., and TAN, H.S.: 'Improved three-dimensional ray tracing technique for microcellular propagation models', *Electron. Lett.*, 1995, **31**, (17), pp. 1503-1505
4 DURGIN, G.D., PATWARI, N., and RAPPAPORT, T.S.: 'An advanced 3D ray launching method for wireless propagation prediction'. IEEE 47th Veh. Technol. Conf., Phoenix, AZ, May 1997

High transconductance AlGaN/GaN heterostructure field effect transistors on SiC substrates

Q. Chen, J.W. Yang, M.A. Kahn, A.T. Ping and I. Adesida

Indexing terms: Silicon carbide, Field effect transistors

Heterostructure field effect transistors have been fabricated using AlGaN/GaN heterostructures grown on *n*-type SiC substrates. These 0.25μm-gate devices exhibited a high drain current and DC transconductance of 1.71A/mm and 222 mS/mm, respectively. In sharp contrast to the high current density HFETs fabricated on sapphire substrates was the absence of the negative differential resistance in the drain characteristics. A drain-to-gate breakdown voltage of 39V was also obtained.

There is a strong interest in the development of AlGaN/GaN based field effect transistors (HFETs) for high power and high temperature applications. This has led to a rapid improvement in the performance of HFETs. DC transconductances as high as 142 [1] and 210mS/mm [2] have been reported. These HFETs have also exhibited a high drain-gate breakdown voltage of 230V [3] and a maximum drain current of 1.02A/mm [1]. The excellent power capability at microwave frequencies has recently been demonstrated by Chen *et al.* with a maximum power of 1.7W/mm at 8.4GHz [4]. While these results have all been obtained on AlGaN/GaN structures grown on sapphire substrates, the low thermal conductivity of the substrate is expected to become the limiting factor for a fully implemented power device. Recently, AlGaN/GaN high electron mobility transistors (HEMTs) have been reported using SiC as the substrates with a transconductance of 70mS/mm and f_t and f_{max} of 6 and 11GHz, respectively [5]. With its high thermal conductivity, SiC substrate material is considered to be more suitable for high power devices. In this Letter, we report on high transconductance and high current density HFETs fabricated on AlGaN/GaN heterostructures grown on SiC. The measured transconductance of 222mS/mm and drain current